Applied Catalysis B: Environmental 166–167 (2015) 155–165

Contents lists available at ScienceDirect

Applied Catalysis B: Environmental

journal homepage: www.elsevier.com/locate/apcatb

Pt electrodeposited over carbon nano-networks grown on carbon paper as durable catalyst for PEM fuel cells

Emanuela Negro[a,1], Roman Latsuzbaia[a,1], Maurizio Dieci[b], Ivo Boshuizen[a], Ger J.M. Koper[a,*]

[a] Department of Chemical Engineering, Delft University of Technology, Julianalaan 136, 2628BL Delft, The Netherlands
[b] CarbonX, Julianalaan 136, 2628BL Delft, The Netherlands

ARTICLE INFO

Article history:
Received 2 September 2014
Received in revised form 31 October 2014
Accepted 8 November 2014
Available online 15 November 2014

Keywords:
Carbon
Platinum
Electrodeposition
Fuel cells
Durability.

ABSTRACT

We propose an innovative 3-step manufacturing technique for the synthesis of the catalyst layer of proton exchange membrane electrodes directly over a gas diffusion layer consisting of carbon paper (CP). In the first step, a carbon synthesis catalyst was formed in a bicontinuous microemulsion. In the second step, carbon nano-networks (CNNs) were directly grown over CP by thermal chemical vapor deposition of ethene over the metal catalyst embedded in the simultaneously carbonized microemulsion matrix. In the third step, the electrocatalyst, here Pt, was deposited on the CNNs. The influence of surfactant type, Na-AOT or Triton X-100, carbon synthesis catalyst type, Fe, Co or Pt, and loading on the electrolyte accessible surface area (ESA) and carbon corrosion resistance was evaluated in a three-electrode half-cell. CNNs grown from Fe and synthetized in Na-AOT microemulsions resulted as the best combination in terms of ESA and carbon corrosion resistance and were used for subsequent investigations. The CNNs grown on CP (CNNs/CP) were electrochemically oxidized prior to Pt electro-deposition by means of potential cycling. The effect of oxidation of the CNNs on the size and spatial distribution of the electrodeposited Pt catalyst was evaluated. Increasing the number of functionalizing oxidation cycles from 0 to 100 decreased the average catalyst crystallite size from 19 to 9 nm. The CNNs/CP samples showing the highest electrochemically active surface area (ECSA) were compared to a commercial catalyst with respect to ECSA, catalyst utilization, and durability to potential cycling. The ECSA for the CNNs/CP samples turned out to be lower than that of the commercial catalyst due to the larger catalyst size. On the other hand, the CNN/CP samples proved to be more durable and higher Pt utilization was achieved.

1. Introduction

Fuel cells are considered to be the green power sources of the twenty-first century and represent the way through which the "hydrogen economy" could become a reality [1]. Proton exchange membrane fuel cells (PEMFCs) are devices in which hydrogen and oxygen electrochemically react to form water by producing electricity and heat. Their biggest advantages over internal combustion engines are no or low CO_2 emissions depending on the hydrogen source, efficiency up to 80%, silent and low-temperature operation, no moving parts and thus long mechanic life-time and no need of lubricants [2–4]. These advantages make PEMFCs promising alternatives to fossil fuel combustion engines both for portable and stationary combined heat and power applications [5]. The main issues preventing their mass-scale commercialization are their cost and their durability that are not yet meeting worldwide-targeted requirements. These issues are closely related to the PEMFC electrodes.

At the electrodes, the electrochemically catalyzed reduction of oxygen (cathode) and oxidation of hydrogen (anode) takes place. The catalyst active sites, Pt nanoparticles (NPs), need to be connected both to a proton-conductive phase, formed by an ionomer, and an electron-conductive phase, formed by a high surface area carbon support. Additionally, the catalyst layer has to be porous to allow the reactants to reach the active sites and the products to leave them [6]. Nowadays, conventional PEMFC electrodes are manufactured by mixing these phases to form an ink that is subsequently distributed, e.g. by spraying or blading, over the gas diffusion layer, usually carbon paper (CP) or carbon cloth [7]. In spite of considerable world-wide effort on optimization, state-of-the-art electrodes still suffer from sub-optimal Pt utilization as well

* Corresponding author.
E-mail address: g.j.m.koper@tudelft.nl (G.J.M. Koper).
[1] These authors had equal contributions to the manuscript.

http://dx.doi.org/10.1016/j.apcatb.2014.11.017
0926-3373/

as large transport losses [8]. This is mainly due to the lack of control of the simultaneous platinum accessibility to reactants, to hydrogen ions transported through the proton-conductive ionomer, to oxygen fed as gas at the cathode and to electrons transported through the conductive carbon support [9,10]. In manufacturing the optimal electrode, several parameters, such as the composition of the catalyst itself, the electrocatalyst loading, the ionomer content and porosity, must be investigated [11,12].

One of the ways to improve catalyst utilization is offered by electro-deposition (ED) techniques to prepare Pt NPs [13]. In the first place, all the electro-deposited NPs have to be in contact with the carbon support and also reachable by reactants, otherwise ED could not have taken place. Secondly, ED mostly happens on the outer surface of the carbon support, due to its hydrophobicity, thereby improving contact with the proton exchange membrane when the PEMFC is assembled [13]. This also allows lowering Pt content in the fuel cell electrode (<0.1 mg cm^{-2}) [14], due to its high utilization and avoiding Pt losses in the depth of the catalyst layer as normally happens with conventional electrode preparation methods, such as pasting and spraying [14]. At the same time, the hydrophobicity of the carbon support also often leads to poor contact with the electro-plating solution, and the resulting loading of Pt NPs on the support is often low with poor spatial distribution [15]. In order to tackle this problem, the carbon support is often functionalized. During this functionalization, by chemical treatment [16–18] or by electrochemical potential cycling [19], defects and functional groups, such us carbonyl, carboxyl and hydroxyl [17], are introduced on the carbon substrate which act as anchoring points for the ED process. In general, although a large amount of work on ED of platinum on carbon supports has been reported, the preparation of a controllable, highly dispersed loading of platinum on a carbon support still poses a challenge to the scientific community.

The durability of PEMFCs at ideal steady-state conditions has already met life-time targets. The degradation rates, however, can increase by several orders of magnitude when conditions include load cycling, start–stop cycles, low humidification or humidification cycling, fuel excess or fuel starvation [9]. Subject to these conditions, the electrochemically active surface area (ECSA) of the catalyst decreases because of (i) NP migration and sintering, (ii) Pt dissolution and redeposition at lower potentials, either in the membrane or on bigger Pt NPs, a phenomenon known as Ostwald ripening, and (iii) carbon corrosion that can cause catalyst detachment. Thermodynamically, carbon can be oxidized to CO_2 even at low potentials [9], but in practice it has been shown to occur at potentials higher than 0.8 V at PEM operating temperatures due to slow kinetics [20]. Therefore, at dynamic fuel cell operating conditions, carbon surface oxides form [9], thereby reducing the hydrophobicity of the support, which can cause the flooding of the electrode [20–22]. Moreover, Pt catalyzes this oxidation process [9]. In practice, the complete oxidation of carbon to CO_2 in Pt/C systems is a two-step process of which the final step requires potentials above 0.8 V [9]. Apart from evolution of carbon dioxide, this results in catalyst detachment from the support with consequent loss of electrochemical surface area (ECSA). Thus, improving the resistance to corrosion of carbon supports is of crucial importance as it is the main cause of performance degradation in low-temperature fuel cells [9,20,23–25]. Recent studies have shown that graphitic materials, such as carbon nanotubes (CNTs) and carbon nanofibers (CNFs), are better alternatives to carbon black supports in terms of corrosion resistance, due to the higher stability of the sp^2-hybridized carbon [9,20,26–28]. On the other hand, relatively inert surfaces have been addressed as a drawback for the use of these materials as support because of their very weak interaction with catalyst NPs and thus weaker bonding of the catalyst [29]. Controlled introduction of defects on the surface such as carboxylic groups can be beneficial since these act as anchoring points for the Pt NPs [30–32]. This allows for better attachment of Pt NPs as well as control over spatial distribution and size of NPs during their synthesis.

By means of thermal chemical vapor deposition (CVD) process, graphitic materials such as CNTs and CNFs were successfully grown on CP. These electrodes were either functionalized with Pt or noble metal NPs for fuel cell applications or as sensors [11,17,33,34]. It was anticipated that this new preparation technique would reduce the electrode fabrication steps, improve the through-plane electrical conductivity, support-diffusion layer and could avoid the decrease in active surface area as in conventional catalyst pasting process [11,17,33–35]. Additionally, fuel cell electrodes based on multiwalled CNTs, which have similar properties to CNNs as we shall discuss later, show superior durability and catalyst utilization compared to conventional carbon black supports [36].

To sum up, PEM electrode cost can be effectively decreased by developing manufacturing techniques involving (i) ED of Pt catalyst and (ii) direct growth of catalyst support on CP, allowing for a better control and a higher Pt catalyst utilization. Additionally, PEM electrode durability can be improved by preventing (i) catalyst agglomeration through anchoring the Pt NPs to the carbon surface and (ii) carbon corrosion by using material with a higher degree of graphitic carbon.

Within our group, we developed a novel carbon material that consists of networked carbon nanostructures, called carbon nanonetworks (CNNs), which is currently produced by a TU Delft spin-off company Carbon X [37,38]. CNNs are carbon graphitic structures organized in a nano-scale pattern. They can be easily produced by CVD of ethene over transition metal catalyst that itself is synthetized in bicontinuous microemulsions (BMEs) [39,40]. The formation of the networked, sponge-like, carbon graphitic structures is due to the carbonization of the surfactant, being the primary carbon source. CNNs show attractive properties for catalysis of fuel cells such as high specific surface area, high electrical conductivity, great oxidation resistance, surface defects increasing the material ability to disperse in solution and to simplify integration into polymer matrices [38]. The versatility and simplicity of the synthesis route promises a less costly production than CNTs. In a previous study, they showed more durable performance than commercial carbon supports in PEM fuel cell applications [28].

In this work, we propose an electrode manufacturing technique consisting of direct growth of CNNs on CP, electrochemical functionalization and decoration with Pt NPs via ED, thereby aiming at a reduction of electrode cost and an increase in electrode durability. First, we investigate the influence of the synthesis parameters, e.g. surfactant and metal, on electrolyte accessible surface area and corrosion resistance of CNNs/CP. Secondly, we electrochemically oxidize CNNs in order to improve Pt ED. Effect of oxidation on the size and distribution of electrodeposited Pt NPs is evaluated. Finally, we compare our best electrocatalyst to a commercial catalyst, with respect to catalyst utilization and durability during potential cycling. CNNs and the proposed manufacturing technique are expected to lead to a (i) higher catalyst utilization, (ii) a more durable catalyst preventing NPs migration and carbon corrosion, (iii) a better connection and distribution of graphitic catalyst support to CP and (iv) reduced manufacturing cost.

2. Experimental

2.1. Materials

Chemicals were purchased from Sigma-Aldrich BV if not otherwise specified and used as-received: the surfactants, sodium bis(2-ethyhexyl)sulfosuccinate (Na-AOT, 99%) and 4-(1,1,3,3-tetramethylbutyl)phenyl-polyethylene glycol (Triton-X

100, 99.999%); the solvents, *n*-heptane (99.9%) and toluene (≥99.5%); acetone (Fluka, >99.8%) and ethanol (98%); the metal precursors, chloroplatinic acid hydrate (99.9%), iron chloride (≥99%), cobalt acetate tetrahydrate (99.999%); the reducing agent, sodium borohydride (granular, ≥ 98%); Toray carbon paper (CP; 45360, Alfa Aesar); perchloric acid ($HClO_4$; 70%) and sulfuric acid (H_2SO_4; J.T. Baker, 67%); the commercial catalyst (HISPEC 9100, Alfa Aesar). Water produced by Milli-Q Ultra-Pure-Water system of Millipore BV was used in all sample formulations.

2.2. CNNs growth over CP

The method followed here is based on previous work [37–40]. Briefly, bicontinuous BMEs were prepared by mixing water/Na-AOT/*n*-heptane or water/Triton-X/toluene in the ratio 0.2/0.53/0.27 or 0.2/0.64/0.16, respectively, in weight. For each synthesis, two BMEs were prepared, one containing the metal precursor and one 10 times excess of reducing agent dissolved in the water phase. Concentration of metal precursor ranged from 10 to 200 mM with respect to the amount of aqueous phase in the BMEs. After an arbitrary waiting time of 1 h, they were mixed and left overnight to complete the reaction. The BME containing the catalyst was directly loaded on CP support. CVD was carried out in a quartz tube reactor of inner diameter 80 mm mounted in a 5-zone tube furnace from P-KEM Ltd. BME containing catalyst was placed over the support in the hot-zone of the reactor. For production, the temperature was raised to 700 °C (10 °C min^{-1}) under nitrogen (N_2) flow at 160 ml min^{-1}. Ethene gas (C_2H_4) was introduced at 96 ml min^{-1} for 60 min at 700 °C. Finally, the ethene gas flow was stopped and the reactor was cooled down to room temperature under nitrogen flow. All gases were introduced at atmospheric pressure. CNNs synthetized over CP were washed three times with acetone and water and then used for further analysis.

2.3. Oxidation of carbon support and Pt electro-deposition

Electrochemical functionalization on the CNNs grown on CP (CNNs/CP) was performed in order to improve attachment and ED of Pt NPs. Experiments were conducted in a conventional three-electrode cell, using a reversible hydrogen electrode (RHE) as reference and a Pt wire as counter electrode. The working electrode was formed by the CNNs/CP samples loaded in a Teflon mask of area 1 cm^2 and in contact with a copper wire on the back. The electrolyte was 3 M H_2SO_4. Potential cycling between 0.64 and 1.34 V vs. RHE at a scan rate of 20 mV s^{-1} was performed for the functionalization of the CNNs, according to the procedure described in [15]. In this range, partial carbon oxidation takes place and the electrical double layer capacitance (DLC) increases due to the formation of functional groups on the carbon surface [41]. The samples are characterized by cyclic voltammetry (CV) measurements before and after oxidation in which way the DLC increase can be monitored. CNNs/CP samples were oxidized for 0, 10 and 100 cycles.

For ED, the same electrochemical setup as for functionalization was used. The precursor solution and electrolyte consisted of 2.5 mM H_2PtCl_6 and 0.5 M H_2SO_4. H_2PtCl_6 was chosen as precursor salt because its high water solubility and previously gave good results for ED [42]. The commonly reported voltage ranges for platinum ED (−0.2 to 0 V vs RHE) often with a minimum negative potential where hydrogen evolution starts [42,43], led to extremely low platinum loading. Hence, lower potentials were chosen in order to improve platinum loading: ED was performed by a voltage pulse of −0.4 V vs. RHE for 60 s, while at rest the voltage was kept at 0.8 V vs. RHE in order to avoid electroless deposition. The temperature in the lab is always in the range between 20 and 22 °C.

2.4. Electrochemical characterization

CV was performed to determine the electrolyte accessible surface area (ESA) of the CNNs/CP and the ECSA of the Pt-CNNs/CP, respectively. The experiments were conducted using the same setup as described above for functionalization and ED. Measurements were carried out with a scan rate of 50 mV s^{-1} in a potential window of 0.05–1.1 V vs. RHE. For the results presented in Fig. 2 and Table 1, 0.5 M H_2SO_4 was used as electrolyte while for results presented in Fig. 4a, 0.1 M $HClO_4$ was used as electrolyte.

ESA was calculated using the DLC as described above assuming a constant number of functional groups directly after CNN synthesis. DLC was determined in a voltage range where no oxidation/reduction peaks were observed. Depending on the sample, a voltage between 0.6 and 0.75 V vs. RHE was chosen and the contribution of the peaks was subtracted.

ECSA was calculated from CV in 0.1 M $HClO_4$ and scan rate of 20 mV s^{-1} as described above, from the hydrogen absorption and desorption regions, after subtracting the contribution of the DLC and the support characteristic peaks as described previously [44].

Accelerated durability tests (ADTs) were carried out by scanning the potential between 0.6 and 1.2 V at a rate of 50 mV s^{-1} in 0.1 M $HClO_4$ saturated with N_2. ECSA was measured every 300 cycles as described previously. Electrochemical carbon corrosion tests on CNNs/CP were conducted by means of potential holding (1.4 V vs. RHE) for 3600 s in 0.5 M H_2SO_4, saturated with N_2, as done in previous work [24]. ECSA was measured after the test as described previously.

2.5. Instrumentation

Transmission electron microscopy (TEM) was carried out using a Philips electron microscope CM300UT-FEG with a point resolution of 0.17 nm, information limit of 0.1 nm, operated at 200 kV. Images were acquired with TVIPS CCD camera. Scanning electron microscopy (SEM), conducted with a JSM-6010LA microscope from JEOL with an energy-dispersive spectrometer (EDS), was used to investigate the structural morphologies of the samples and to perform elemental analyses. Thermogravimetric analysis (TGA) was performed in N_2 with a Mettler-Toledo instrument to quantify the weight loss of CP during CVD. X-ray photoelectron spectroscopy (XPS) measurements were performed on a Thermo Fischer Scientific (K Alpha model), equipped with a monochromatic Al Kα X-ray source. The measurements were carried out in normal emission with a spot size of 400 μm and pressure of 10^{-9} bar. In order to compensate for the surface charging the flood gun was enabled during the measurement. The obtained spectra were analyzed with Avantage processing software. X-ray diffraction (XRD) is used to show the presence of Pt NPs and in case of sufficient loading, to determine NP size. The size has been calculated from the Scherrer equation. XRD measurements have been conducted on a Thermo Bruker AXS with a cobalt source.

3. Results and discussion

3.1. Influence of CNNs synthesis parameters on ESA and corrosion resistance

CNNs were synthetized by thermal CVD of ethene over metal NPs, Fe, Co or Pt, synthetized in BME composed by water/Na-AOT/*n*-heptane or water/TritonX-100/toluene [37,38]. Fe, Co and Pt NPs size was circa 2–3 nm [39,40]. Catalyst synthetized in BMEs were cast directly over CP. A summary of the synthesis details of samples produced, metal and carbon loading is reported in Table 1. Metal loading was calculated from a balance of mass, and CNN loading was

Table 1
Summary of CNNs/CP synthesis parameters, metal and CNNs loading, mass-specific capacitance and ESA gain, carbon corrosion fitting parameters and charge exchanged.

Sample	Surfactant	Metal	Metal density ($\mu g\,cm^{-2}$)	CNNs ($mg\,cm^{-2}$)	Mass spec. cap. ($F\,g^{-1}$)	ESA Gain	kA ($g^{-1}\,s^{-n}$)	n	DLC AC/BC*	QC (cm^{-2})	Corrosion Index
1	AOT	Fe	2	7.1	2.5	23	0.50	0.16	1.9	5.0	0.04
2	AOT	Fe	14	2.0	5.8	15	1.4	0.17	2.2	6.0	0.08
3	AOT	Fe	37	2.2	7.6	22	0.18	1.5	1.1	3.0	0.03
4	AOT	Co	2	14	0.3	2.6	0.33	0.11	2.5	4.8	0.4
5	AOT	Co	4	14	0.5	4.9	2.0	0.23	1.6	4.4	0.2
6	AOT	Pt	12	0.52	25	17	7.2	0.23	2.6	5.1	0.06
7	TX	Pt	6	1.1	0.7	1.0	1.2	0.05	3.0	3.6	0.7
8	TX	Pt	18	1.2	1.9	2.9	2.2	0.63	1.7	3.4	0.2
9	TX	Pt	42	1.0	4.9	6.4	1.4	0.05	4.2	3.4	0.10
Surface-specific capacity ($F\,cm^{-2}$)											
CP	–	–	–	–	0.002	–	–	–	1.7	5.1	1

* DLC before and after corrosion.

calculated from the difference in weight of the CNNs/CP with bare CP that undergoes the same heat treatment. From TGA measurements in N_2, CP loses circa 25% of weight because of heat treatment. BME type, metal and metal concentrations were varied in order to identify the best conditions to (i) increase CP surface area in order to allow a better distribution of Pt NPs later on and (ii) obtain high corrosion-resistant supports.

Fig. 1a–d shows SEM images of CNN/CP produced from Fe synthetized in AOT BMEs. Homogeneous coverage of the CP with CNNs was achieved, as shown in Fig. 1a. CNNs are rod-like structures with an average diameter of 250 nm and length up to several micrometers. Due to the high density of growing structures, CNNs interconnect with each other (Fig. 1d). The mechanism of formation of CNNs has been extensively studied elsewhere [37,38]. CNNs grown from Pt synthetized in Triton X-100 BMEs are ticker, up to 1 μm. This is due to the fact that Triton-X 100 binds less strongly to the surface of the catalyst NPs and at high temperatures most of it decomposes in volatile products. This causes a partial agglomeration of catalyst NPs before the synthesis resulting in thicker nanostructures [38]. Fig. 1h shows CNNs grown from cobalt synthetized in AOT with a diameter of 300 nm and length up to 1 μm.

CV was carried out as described above to determine the ESA from the measured capacitive current. The ESA was lower than the total surface area, circa $100\,m^2\,g^{-1}$ as measured with BET previously [28,38], because of the different surface properties, functional groups versus gas adsorption, used for its determination. In addition, the electrolyte accessible carbon surface area will always be less because of the relatively low wettability because of which small pores are inaccessible [45]. Examples of CVs of some CNNs/CP are reported in Fig. 2a and b. CVs of bare CP are also reported, to show that ESA increased after the synthesis of CNNs (Fig. 2a). Some redox peaks corresponding to surface defects, such as surface quinones, can be observed. This can be beneficial for catalytic applications [46]. When using Fe as catalyst at the synthesis conditions, higher ESA values were obtained.

Comparison of metal loading, CNN loading and specific ESA is reported in Fig. 3a. In general, keeping the other conditions constant, an increase in metal loading did not vary the CNN loading, as the carbon source (surfactant + ethene) is kept constant (Table 1). This can be seen for samples 4 and 5, Co loading of 2–4 $\mu g\,cm^{-2}$ led to CNNs loading of 14 $mg\,cm^{-2}$, and samples 7–9, where an increase of Pt loading from 6 to 42 $\mu g\,cm^{-2}$ did not affect the quantity of CNNs produced, circa 1 $mg\,cm^{-2}$. However, increase in metal loading did cause an increase in mass-specific capacitance. The larger number of nucleation points brought about by more catalyst NPs for CNN growth led to thinner structures when the carbon feed is kept constant, leading to an increased surface area. Thus, for iron the mass-specific capacitance increased from 2.5 to 7.6 $F\,g^{-1}$, samples 1–3, for cobalt from 0.3 to 0.5 $F\,g^{-1}$, samples 4 and 5, for Pt from 0.7 to 4.9 $F\,g^{-1}$, samples 7–9. In general, CNNs grown from NPs synthetized in Na-AOT BMEs led to higher ESA, as is clear from samples 6 and 7-8-9, where CNNs from Pt synthetized in Na-AOT show a specific mass capacitance at least one order of magnitude

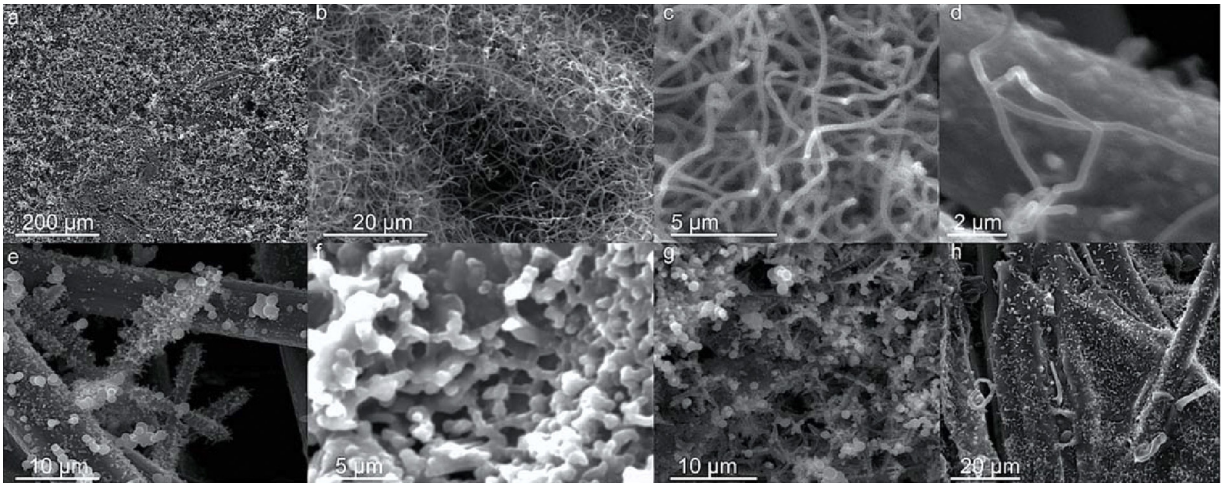

Fig. 1. SEM images of CNNs/CP: (a–d) different magnifications of sample 2, grown from Fe synthetized in Na-AOT microemulsion; (e–g) samples 7–9, respectively, grown from Pt synthetized in Triton-X100 microemulsion, (h) sample 5, grown from Co synthetized in AOT.

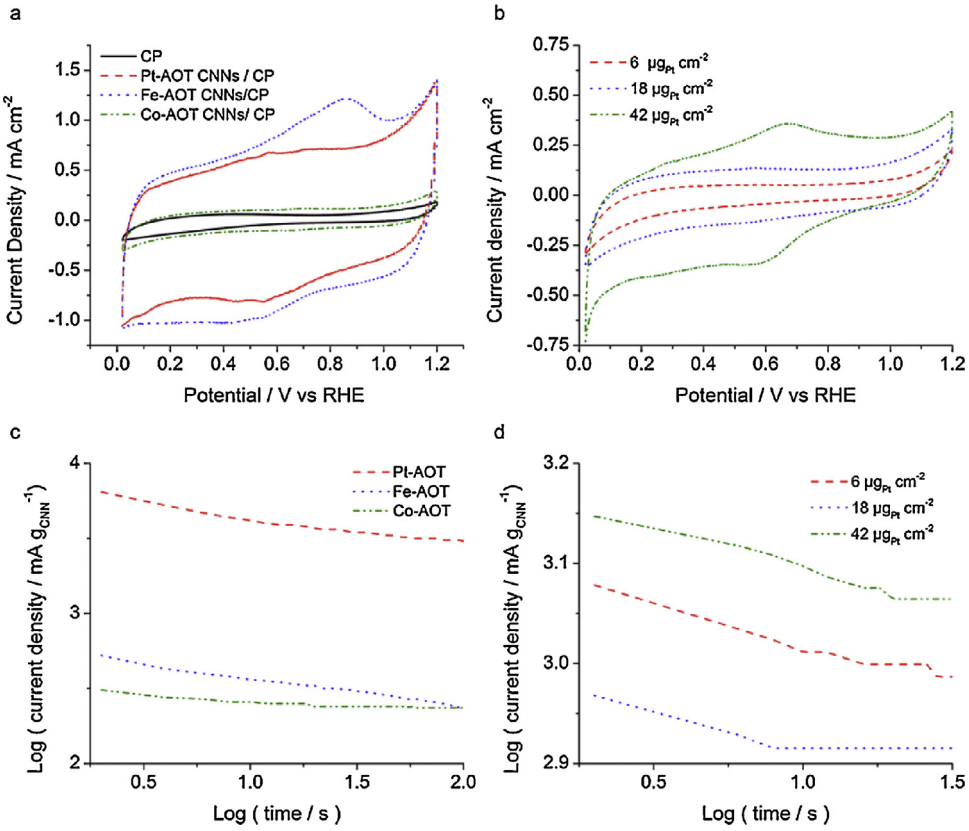

Fig. 2. CVs of (a) bare CP and samples 1, 4 and 6 and (b) samples 7–9. Double logarithmic plots of current density versus time for (c) bare CP and samples 1, 4 and 6 and (d) samples 7–9.

larger than those synthetized in Triton X-100 BMEs. This is because AOT binds strongly to the metal surface, thereby preventing catalyst agglomeration during the heating ramp of the reactor. In this way, carbon production is higher due to larger catalyst surface.

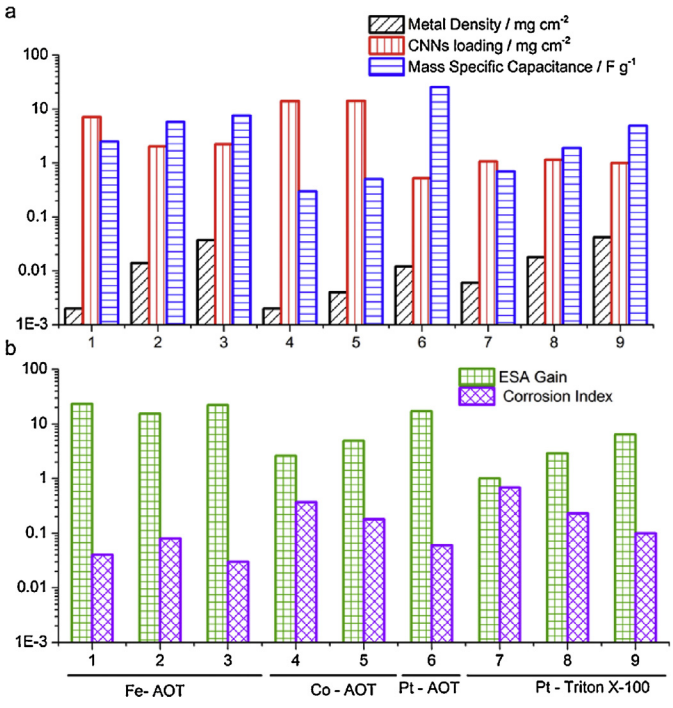

Fig. 3. (a) Mass-specific capacitance, metal and CNN loading; (b) ESA gain and corrosion resistance index.

In order to easily evaluate the efficiency of the synthesis and increase of the support ESA, the ESA gain coefficient was introduced, defined according to Eq. (1):

$$ESA\ \ gain = \frac{ESA_{CNN/CP}}{ESA_{CP}} \quad (1)$$

where $ESA_{CNN/CP}$ is the ESA after the CNNs after synthesis and ESA_{CP} is the ESA of the bare CP, 0.002 F cm^{-2}. Values are reported in Table 1.

The other key parameter, corrosion resistance, was also evaluated by electrochemical methods. Carbon corrosion experiments were conducted in a three-electrode cell by means of potential holding (1.4 V vs RHE) for 60 min and measuring exchange current density as a function of time. Carbon corrosion takes place at potentials larger than 0.207 V vs. RHE according to Eq. (1) and the current–time, j–t, behavior is generally described according to Eq. (2):

$$j = kt^{-n} \quad (2)$$

where k and n are the corrosion rate coefficient and the order of corrosion reaction, respectively [24]. Fig. 2c and d shows log j vs. log t curves from which the parameters, k and n, were extracted. The charge exchanged over 60 min and the extracted parameters k and n are summarized in Table 1.

From Fig. 2c, one may observe that the corrosion rate for CNNs synthetized from Pt is higher than the one synthetized from Fe and Co. This might be due to the fact that part of the metal surface is available to the electrolyte and it is active in catalyzing the corrosion of carbon as well. Pt is indeed a strong catalyst for carbon corrosion. Previous studies show that corrosion in PEM electrodes measured as CO_2 evolution is proportional to the Pt–carbon contact area [9]. However, no hydrogen absorption peaks and Pt surface

Table 2
Surface composition and concentration of functional groups from the deconvolution of peaks from C 1s regions in the XPS spectra (Fig. 5).

	Composition from the survey (at%)		Composition from deconvoluted C1s spectra (at%)			
	C	O	C–O (285.9 eV)	C=O (287.2 eV)	O–C=O (288.3 eV)	π–π* (291.0 eV)
CNN0	85	15	45	6.3	29	20
CNN10	78	22	59	3.2	29	8.9
CNN100	80	20	37	29	23	12
CP*	99	1.3	–	–	–	–

* Analysis performed on reference empty CP before the growth of the CNNs.

area could be determined from CV measurements (see Fig. 2a and b), but this might be due to the low amount of Pt in the sample. Corrosion also depends on the amount of defects present in the CNN samples. Another possibility is therefore that CNNs grown from Pt exhibit more defects and are thus more easily corroded. Raman measurements, usually reported to quantify the amount of defects in graphitic materials, were performed for these samples but were not informative because of the larger contribution from the CP.

Pt loading has a controversial effect on the corrosion resistance, as can be observed from Fig. 2d. Corrosion rate is minimal for sample 8, produced from 18 μg cm^{-2}, higher for sample 7, produced from 6 μg cm^{-2}, and even higher 42 μg cm^{-2}. Pt catalyzes the formation of graphitic structures during the CVD, which are more resistant to carbon corrosion, as well as the corrosion of carbon itself during the corrosion tests. Sample 8, having the minimum corrosion rates, represented the optimum balance between these two counteracting effects.

After corrosion, ESA increased due to an increased amount of defects on the surface and an increased roughening of the surface. The ratio of DLC after and before corrosion is reported in Table 1 for the various samples. Similarly, higher ESA increase was achieved with Pt catalyst.

In order to evaluate the corrosion resistance in a straightforward manner, a corrosion index is introduced according to Eq. (3):

$$\text{Corrosion index} = \frac{Q_{CNN/CP}}{Q_{CP}} \frac{ESA_{CP}}{ESA_{CNN/CP}} \quad (3)$$

where $Q_{CNN/CP}$ is the corrosion charge for the CNN/CP samples, while Q_{CP} is the corrosion charge of the bare CP. The corrosion index is normalized with the ESA gain to take into account that higher ESA are obviously leading to higher exchanged current. Values are reported in Table 1. The corrosion index decreased with increasing metal loading, as it is clearly noticeable for samples 4 and 5 and samples 7–9 in Fig. 3b.

In order to have the best catalyst support, a high ESA gain and low corrosion index are necessary. From Fig. 3a, the best catalyst support was sample 3, CNNs/CP grown from iron. Therefore, sample 3 was used for further experiments and tested as support for Pt electrodeposition.

3.2. Electrodeposition of Pt over CNN/CP: effect of functionalization

3.2.1. Functionalization

Non-functionalized carbon supports are characterized by a very low surface energy, which means that physically or chemically deposited NPs on these supports only weakly interact with the support [15]. This has a serious impact on the ED process, as the nucleation of Pt is least favorable on such hydrophobic surfaces. For instance, it is observed in the literature [47] and our work that during the ED process of Pt on highly ordered pyrolytic graphite (HOPG) supports, NPs mainly nucleate on cracks and defects rather than on smooth HOPG planes. Similar effects can be observed while depositing on pristine CNNs. Therefore, in order to improve attachment of Pt on graphitic supports and increase the number of nucleation points, defects were introduced by partial electrochemical oxidation of the CNNs. In order to achieve this, potential cycles between 0.641 and 1.341 V were applied in 3 M H_2SO_4 at 20 mV s^{-1}. The degree of functionalization was monitored by measuring the DLC of the carbon surface in $HClO_4$ [48]. When oxidizing the surface, the DLC of the carbon support increases by both roughening, due to the removal of amorphous carbon, and by introduction of charged surface groups [48]. Fig. 4a and b shows the CVs after different degrees of oxidation and the increase of the DLC with potential cycling, respectively.

In order to investigate the nature of the functional groups, XPS measurements were performed. The carbon-to-oxygen weight ratios were extracted from the XPS spectrum (Fig. 5a) and are summarized in Table 2. The oxygen content of the surface of bare carbon paper is only 1.3%, but after CNN growth, the oxygen content increased to 14.6%. CNNs contain oxygen as a result of the carbonization of the surfactant [38]. The functionalization leads to further increase of the oxygen content to 22% for CNN10. Further oxidation up to 100 cycles (CNN100) leads to slightly lower, 20%, oxygen content. The amount of the functional groups is slightly decreased most likely because of some further oxidation of functional group to CO_2 [9]. Therefore, there is an optimum number of oxidation cycles for the functionalization of the support.

The relative concentration of oxygen functional groups on the surface of the CNN/CP support was determined by deconvolution of the XPS C1s spectra (see Fig. 5b–d). Curves fitted to the C 1s spectra had their peak position for C–C bonds of the graphitic material at 284.3 eV, phenol and ether groups (C–O) at 285.9 eV, carboxyls, carboxylic anhydrides and esters (O–C=O) at 288.3 eV, carbonyl, aldehydes and quinones (C=O) at 287.2 eV, and the characteristic shake-up line of aromatic carbon (π–π*) at 191.0 eV [49]. The predominant oxygen functional groups were C–O, however with prolonged oxidation, sample CNN100, C–O and O–C=O content decreased while C=O increased. It is important to mention that the amount of carboxylic groups did not vary significantly and is quite high compared to what is reported in the literature [49]. No iron was detected by XPS. As this is a surface technique with a penetration depth of 8–10 nm [50], it is hence concluded that iron is located inside the carbon structure or leached out during oxidation cycles in 3 M H_2SO_4. The electrochemical response around 0.7 V, as visible from the CV in Fig. 4a, is therefore probably due to surface quinones [40].

EDS mapping of the supports before and after oxidation is represented in Fig. 6a–f. It is observed that the oxygen is present on the CNN/CP support both in CNNs and the fibers of CP. Also, the

Table 3
Elemental quantification of C, O and Fe from EDS after functionalization.

Sample	EDS Composition (wt%)		
	C	O	Fe
CNN0	95.2	4.2	0.5
CNN10	94.1	5.5	0.4
CNN100	95.0	4.7	0.3

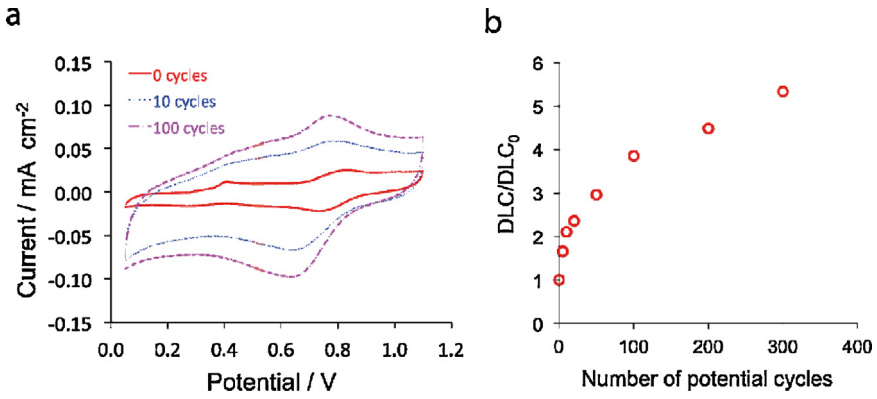

Fig. 4. (a) CVs from CNNs/CP samples of different degree of oxidations. Double-arrowed vertical bar indicates the direction of DLC increase with oxidation cycles. (b) Relative increase of DLC as a function of number of oxidation cycles.

oxygen is present even before oxidation. Table 3 summarizes the concentrations of the components of the supports after oxidation. Arguments similar to XPS discussion can be used to explain oxygen content differences in the samples. The values of oxygen are roughly four times lower than the values detected by XPS because of much higher penetration depth of the EDS [50,51]. Indeed oxygen is expected to be only present on the surface.

3.2.2. Electrodeposition

Fig. 7a shows the currents achieved during the ED process. As concluded from the XPS measurements, CNN10 and CNN100 had almost equal amounts of functional groups, whereas non-functionalized samples had a much lower content of functional groups. In Table 4, the degree of functionalization of the CNNs is summarized by means of the relative increase in DLC, DLC/DLC_0. There is a clear trend of increasing DLC leading to a higher amount of Pt deposited as well as to smaller NPs. This is also clearly observed in Fig. 7a, where higher currents were recorded during ED over CNN10 and CNN100. Therefore, larger amounts of NPs were deposited on the sample with the larger amount of anchoring points on the carbon surface. This also resulted in a higher ECSA, as can be seen from the peaks for hydrogen adsorption and desorption in the voltammograms which increase in the order CNN0–CNN10–CNN100 (see Fig. 7b).

From the XRD patterns, an example is reported in Fig. 8, the peak corresponding to Pt [111]-crystal structure is hardly visible due to the low Pt content in all the samples, whereas carbon peaks are very pronounced. NPs size was calculated with the Scherrer equation for the more pronounced peak, corresponding to Pt [111]. A magnified image of the peak is reported in Fig. 8b and results are reported in Table 4. Increasing the oxidation of the support resulted in a decrease in the crystallite size from 19 to 9 nm. TEM images confirmed the size calculated from XRD (see Fig. 9). A larger number of nucleation points for platinum NPs, obtained with more oxidation

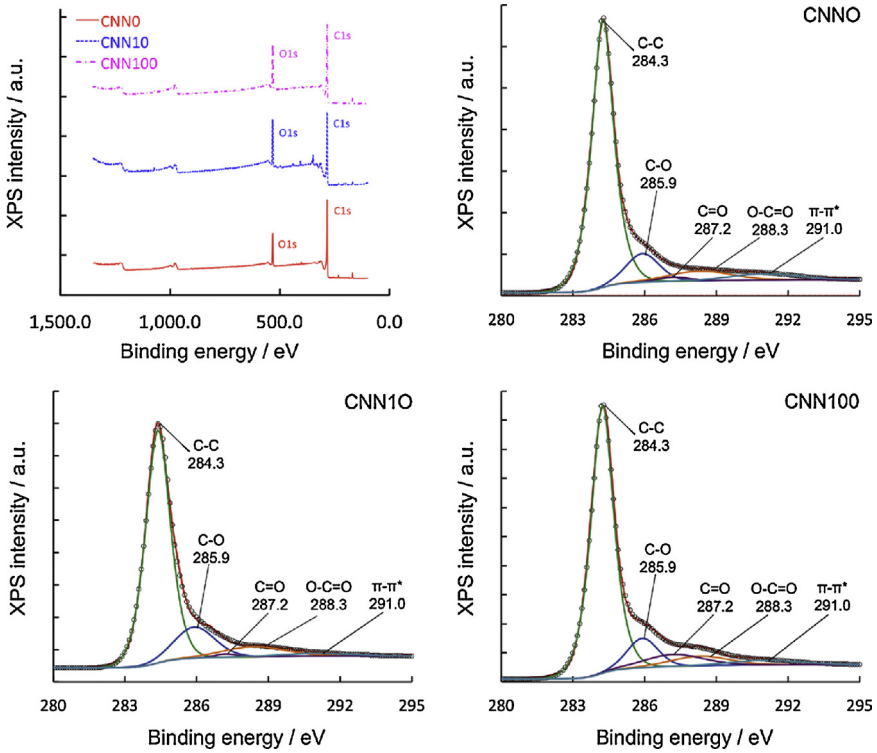

Fig. 5. (a) XPS spectrum of the CNN/CP support as prepared (in red), after 10 oxidation cycles (blue) and 100 oxidation cycles (green). (b–d) Deconvolution of the XPS C 1s peaks of the support before oxidation, after 10 and 100 cycles, respectively.

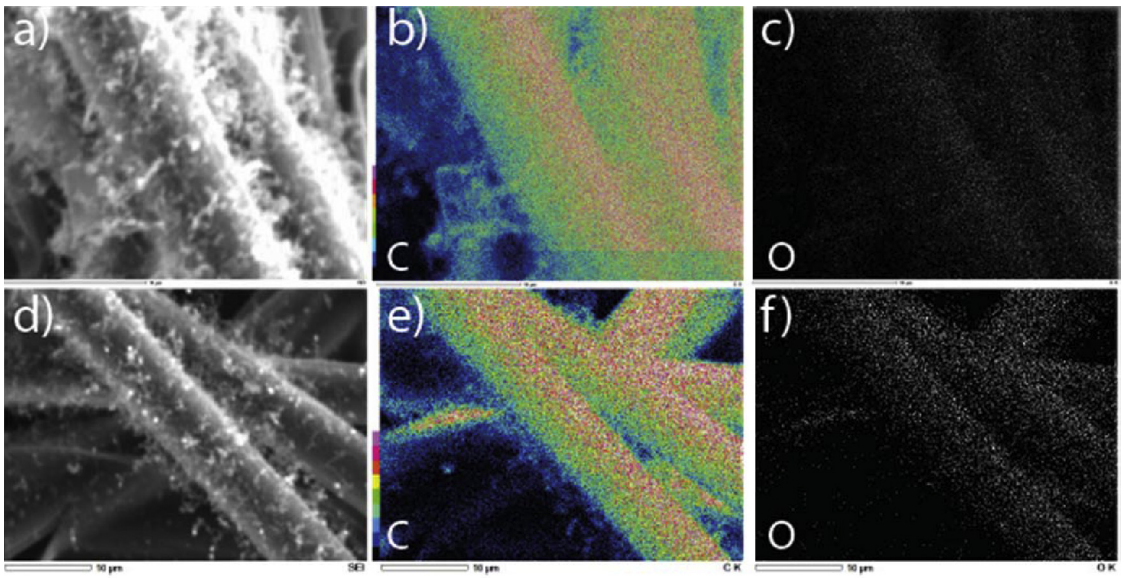

Fig. 6. SEM images of the supports with CNNs directly grown on them (a, d). EDS mapping before oxidation cycles (CNN0)—carbon (b) and oxygen (c)—and after 100 oxidation cycles (CNN100)—carbon (e) and oxygen (f).

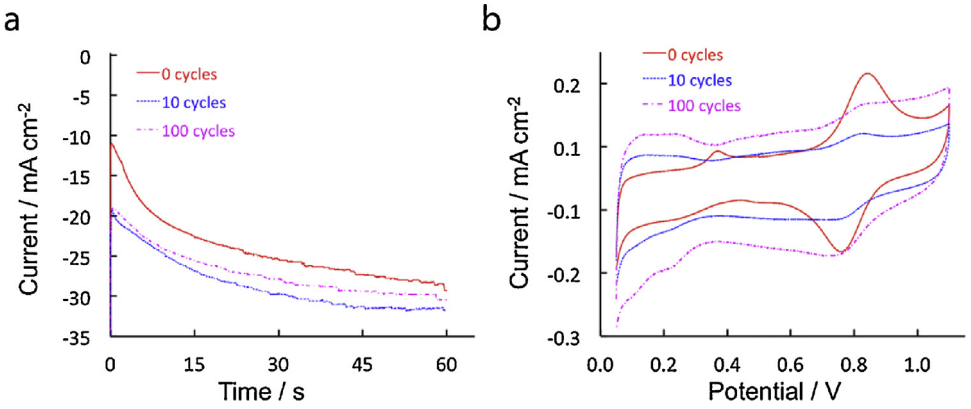

Fig. 7. (a) ED current vs. time for samples CNN0, CNN100 and CNN100, (b) CV of Pt catalyst on CNN0, CNN10 and CNN100, at room temperature in N_2-saturated 0.1 $HClO_4$ solution at 20 mV s^{-1}.

cycles, at equal ED time and conditions, resulted in smaller NPs size and thus larger ECSA.

Due to the low concentrations of Pt on the supports, the loading of Pt by weight difference, thermogravimetric analysis, inductively coupled plasma analysis after acid washing or measurement of the concentration decrease of Pt precursor in the electrolyte as done in other studies [13,17,18] could not be performed. Also, the penetration depth of EDS is in the order of microns, which means that when measuring composition of the catalyst layer, the signal from the CP adds up to the signal of carbon of CNNs. Similarly, XPS with a penetration depth of 8–10 nm does not provide complete information. Therefore, Pt-loading was calibrated by analyzing TEM micrographs of the CNN100 sample, and based on those values the composition of the catalyst layer and the loading of Pt on this and the other supports was determined. These loadings were reliable according to EDS and reported ED efficiencies [52] at the specified conditions and time.

The platinum loading prepared via electrodeposition is in the range of what is reported in the literature, normally varying from 0.05 to 0.3 mg cm^{-2} for the ultralow platinum content electrodes for fuel cells [14]. The loading of Pt on CNNs could be increased by further oxidation of the CNNs, as is obvious from TEM images, therefore, by increasing the amount of anchoring points. On the other hand, ultralow platinum content electrodes are the way to decrease the cost of the fuel cell electrodes [53], high ECSA has to be achieved though.

ECSA was calculated by subtracting the contribution of the support before electrodeposition [28,54]. The best sample in terms

Table 4
Double-layer capacitance, DLC/DLC0, Pt loading, NP size as measured by XRD for the three samples CNN0, CNN10 and CNN100.

Sample name	DLC/DLC_0	Pt wt% from EDS	Pt loading ($\mu g\,cm^{-2}$)	Pt size from XRD (nm)
CNN0	1.0	1.0	13	19
CNN10	2.1	1.9	24	11
CNN100	3.9	2.0	26	9

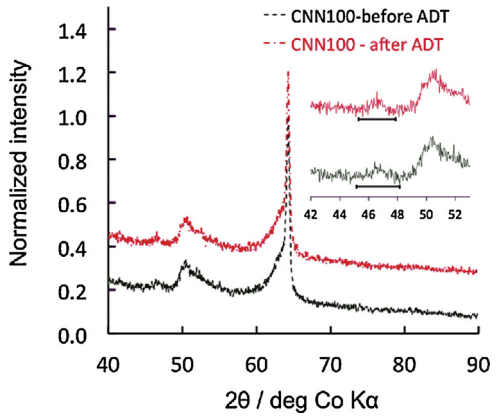

Fig. 8. XRD measurement on the sample CNN100 before and after ADT. Inset shows Pt[111] peak.

of ECSA, 23 $m^2 g^{-1}$, and particle size, 9 nm, was by these criteria CNN100.

3.2.3. Durability tests

Accelerated degradation tests (ADTs) were performed on the electrodes fabricated with the described method. The ADT consisted of 3000 potential cycles in the range of 0.6–1.2 V at 50 mV s^{-1} in 0.1 M $HClO_4$ and 22 °C. In this potential range, all degradation mechanisms take place [9]. NP size was determined before and after the ADT by means XRD (Fig. 8). For all samples, NP size increased due to Ostwald ripening or agglomeration. Results are summarized in Table 5.

ECSA was measured by CV before and after ADT. Due to the low amount of platinum, ECSA variation for samples CNN0 and CNN10 could not be accurately determined. ECSA decreased from 23 to 21 $m^2 g^{-1}$ for CNN100 (Fig. 10a). Interestingly, ECSA initially increased during ADT (Fig. 10c). This is probably due to Pt surface

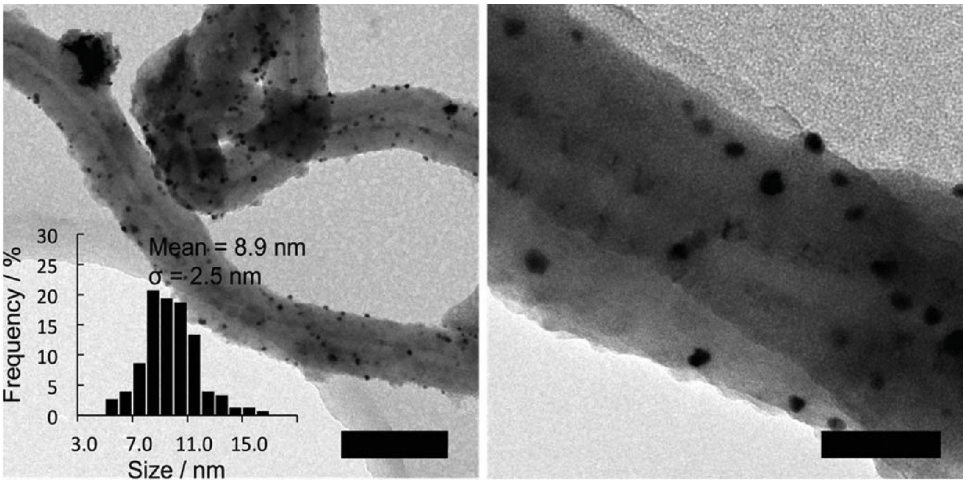

Fig. 9. TEM micrographs of CNN100 sample, scale bar is 200 and 50 nm, respectively.

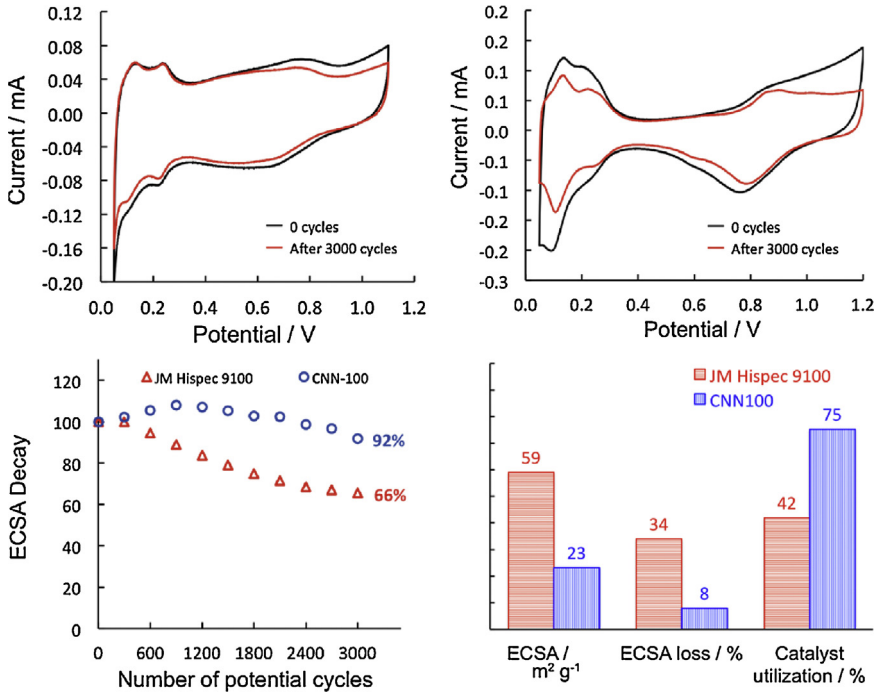

Fig. 10. CV before and after ADT for (a) CNN100 and (b) commercial catalyst; (c) decrease of ECSA with respect to initial value as a function of potential cycling and (d) comparison of CNN100 with commercial catalyst regarding ECSA, ECSA decay and catalyst utilization.

Table 5
ECSA and catalyst particle size before and after ADT.

Sample	ECSA ($m^2\ g^{-1}$)		Pt size (XRD) (nm)	
	Before ADT	After ADT	Before ADT	After ADT
CNN0	n.a.	n.a.	19	20
CNN10	11	n.a.	11	13
CNN100	23	21	9	13

roughening which increases the effective ECSA as observed previously [55]. CNN100 was compared to a commercial electrode undergoing the same ADT treatment (Fig. 10b). A summary of the comparison is reported in Fig. 10d. ECSA for commercial catalyst was much larger due to the smaller catalyst size, about 2.8 nm [28]. CNN100 showed great stability, only 8% ECSA loss observed, whereas in the case of commercial JM Hispec 9100 catalyst, ECSA loss amounted to 34% (Fig. 10c and d). This difference might be attributed to a lower Pt content of our electrode which can catalyze the carbon corrosion, as well as larger NPs size that are more stable. However, previous studies showed that CNN support has higher corrosion resistance than commercial supports [28]. Additionally, the direct growth of CNNs on CP provides a better attachment of the catalyst layer to the CP fibers and therefore the detachment of the CNNs from the carbon fibers due to oxidation is reduced. Furthermore, ED of the NPs provides a better platinum–carbon interaction and prevents catalyst degradation processes such as NP migration and agglomeration and NP detachment [16]. Finally, the electrodeposited NPs are well dispersed on the CNNs, which also reduces agglomeration, and Ostwald ripening and Pt utilization was very high, 75% compared to 42% in commercial catalyst (Fig. 10d).

4. Conclusions

We have successfully developed a novel 3-step manufacturing technique for PEM electrodes, combining the direct growth carbon nano-networks over carbon paper, CNNs/CP, with electrochemical functionalization and platinum deposition. Firstly, we investigated the influence of various synthesis parameters, such as metal type and concentration, surfactant type, on CNN electrolyte accessible surface area and corrosion resistance. We found that CNNs grown from iron using Na-AOT-based microemulsions gave the best performance. We further electrochemically functionalized CNNs/CP supports introducing oxygen containing groups on the surface. Samples with different degrees of functionalization were produced and used for subsequent ED. A higher degree of oxidation led to smaller NPs and a higher loading. This is in accordance with the larger amount of nucleation points being beneficial for both ED efficiency and NPs size. The best sample, having an ECSA of 23 $m^2\ g^{-1}$, was compared to a commercial catalyst in terms of ECSA, catalyst utilization and durability to potential cycling. While ECSA was lower due to larger size of NPs—9 nm compared to 2.8 nm for the commercial catalyst—the resulting catalyst utilization was almost double, 75% compared to 42%. Additionally, it performed better in terms of durability, because of the higher corrosion-resistance, better CNN contact with CP and Pt with CNN due to the ED process. Further optimization of the manufacturing technique, for example, in order to obtain smaller particles and thus increase ECSA, is expected to improve the electrode performance compared to commercial electrodes. Nevertheless, the simplicity of the manufacturing technique and the reduction of manufacturing steps make this novel electrode promising as material for fuel cells.

Acknowledgements

We thank Louw Florusse for TEM micrographs. We acknowledge financial support from the Advanced Dutch Energy Materials (ADEM) Program, the Ministry of Economic Affairs in the Netherlands in the framework of IOP-Self Healing Materials (SHM) Program and the COST CM1101 Action.

References

[1] M. Ball, M. Wietschel, International Journal of Hydrogen Energy 34 (2009) 615–627.
[2] J. Larminie, A. Dicks, Fuel Cell Systems Explained, Second Edition, Wiley, 2003.
[3] X. Cheng, Z. Shi, N. Glass, L. Zhang, J. Zhang, D. Song, Z.-S. Liu, H. Wang, J. Shen, Journal of Power Sources 165 (2007) 739–756.
[4] W. Vielstich, A. Lamm, H.A. Gasteiger, Handbook of Fuel Cells: Fundamentals, Technology and Applications, Vol. 3, 2003.
[5] S. Satyapa, DOE Hydrogen Program—2010 Annual Progress Report, in: U.S.D.o. Energy (Ed.), 2011.
[6] F.A. Bruijn, R.C. Makkus, R.K.A.M. Mallant, G.J.M. Janssen, Advances in Fuel Cells 1 (2007).
[7] S. Litster, G. McLean, Journal of Power Sources 130 (2004) 61–76.
[8] H.A. Gasteiger, S.S. Kocha, B. Sompalli, F.T. Wagner, Applied Catalysis B: Environmental 56 (2005) 9–35.
[9] F.A. de Bruijn, V.A.T. Dam, G.J.M. Janssen, Fuel Cells 8 (2008) 3–22.
[10] M. Lee, M. Uchida, H. Yano, D.A. Tryk, H. Uchida, M. Watanabe, Electrochimica Acta 55 (2010) 8504–8512.
[11] C.H. Wang, H.Y. Du, Y.T. Tsai, C.P. Chen, C.J. Huang, L.C. Chen, K.H. Chen, H.C. Shih, Journal of Power Sources 171 (2007) 55–62.
[12] G. Hoogers, Fuel Cell Technology Handbook, CRC Press, 2003.
[13] M.C. Campagnolo, C.A. Marozzi, A.C. Chialvo, M.R. Gennero de Chialvo, Journal of Power Sources 239 (2013) 207–216.
[14] C. Paoletti, A. Cemmi, L. Giorgi, R. Giorgi, L. Pilloni, E. Serra, M. Pasquali, Journal of Power Sources 183 (2008) 84–91.
[15] C. Xu, J. Chen, Y. Cui, Q. Han, H. Choo, P.K. Liaw, D. Wu, Advanced Engineering Materials 8 (2006) 73–77.
[16] H. Tang, J.H. Chen, Z.P. Huang, D.Z. Wang, Z.F. Ren, L.H. Nie, Y.F. Kuang, S.Z. Yao, Carbon 42 (2004) 191–197.
[17] K. Saminathan, V. Kamavaram, V. Veedu, A.M. Kannan, International Journal of Hydrogen Energy 34 (2009) 3838–3844.
[18] D. Santiago, G.G. Rodríguez-Calero, H. Rivera, D.A. Tryk, M.A. Scibioh, C.R. Cabrera, Journal of the Electrochemical Society 157 (2010) F189–F195.
[19] D.-J. Guo, H.-L. Li, Journal of Electroanalytical Chemistry 573 (2004) 197–202.
[20] R. Borup, J. Meyers, B. Pivovar, Y.S. Kim, R. Mukundan, N. Garland, D. Myers, M. Wilson, F. Garzon, D. Wood, P. Zelenay, K. More, K. Stroh, T. Zawodzinski, J. Boncella, J.E. McGrath, M. Inaba, K. Miyatake, M. Hori, K. Ota, Z. Ogumi, S. Miyata, A. Nishikata, Z. Siroma, Y. Uchimoto, K. Yasuda, K.I. Kimijima, N. Iwashita, Chemical Reviews 107 (2007) 3904–3951.
[21] J.D. Fairweather, B. Li, R. Mukundan, J. Fenton, R.L. Borup, ECS Transactions 33 (2010) 433–446.
[22] R.L. Borup, J.R. Davey, F.H. Garzon, D.L. Wood, M.A. Inbody, Journal of Power Sources 163 (2006) 76–81.
[23] W. Sheng, S. Woo Lee, E.J. Crumlin, S. Chen, Y. Shao-Horn, Journal of the Electrochemical Society 158 (2011) B1398–B1404.
[24] D. Sebastián, A.G. Ruíz, I. Suelves, R. Moliner, M.J. Lázaro, V. Baglio, A. Stassi, A.S. Aricò, Applied Catalysis B: Environmental 115–116 (2012) 269–275.
[25] J.-H. Park, S.-D. Yim, T. Kim, S.-H. Park, Y.-G. Yoon, G.-G. Park, T.-H. Yang, E.-D. Park, Electrochimica Acta 83 (2012) 294–304.
[26] L. Li, Y. Xing, Journal of Power Sources 178 (2008) 75–79.
[27] S.M. Andersen, M. Borghei, P. Lund, Y.-R. Elina, A. Pasanen, E. Kauppinen, V. Ruiz, P. Kauranen, E.M. Skou, Solid State Ionics 231 (2013) 94–101.
[28] E. Negro, M.A.D. Vries, R. Latsuzbaia, G.J.M. Koper, Fuel Cells (2014).
[29] M.S. Saha, A. Kundu, Journal of Power Sources 195 (2010) 6255–6261.
[30] Y. Xing, The Journal of Physical Chemistry B 108 (2004) 19255–19259.
[31] C. Xu, J. Chen, Y. Cui, Q. Han, H. Choo, P.K. Liaw, D. Wu, Advanced Engineering Materials 8 (2006) 73–76.
[32] H. Wu, D. Wexler, G. Wang, H. Liu, Advanced Science Letters 4 (2011) 115–120.
[33] M.-C. Tsai, T.-K. Yeh, C.-H. Tsai, Electrochemistry Communications 8 (2006) 1445–1452.
[34] X. Yue, S. Pang, P. Han, C. Zhang, J. Wang, L. Zhang, Electrochemistry Communications 34 (2013) 356–359.
[35] K.-C. Pham, D.H.C. Chua, D.S. McPhail, A.T.S. Wee, ECS Electrochemistry Letters 3 (2014) F37–F40.
[36] L. Li, Y. Xing, Journal of Power Sources 178 (2008) 75–79.
[37] K.N.K. Kowlgi, G.J.M. Koper, R.A.D. Van Raalten, Carbon Nanostructures and Networks produced by Chemical Vapor Deposition, Delft Enterprises. B.V. (Ed.), 2012.
[38] E. Negro, M. Dieci, D. Sordi, K.N.K. Kowlgi, M. Makkee, G. Koper, Chem. Commun. 50 (2014) 11848.
[39] E. Negro, R. Latsuzbaia, G.J.M. Koper, Langmuir 30 (2014) 8300–8307.
[40] K. Kowlgi, U. Lafont, M. Rappolt, G. Koper, Journal of Colloid and Interface Science 372 (2012) 16–23.

[41] C. Li, D. Wang, X. Wang, J. Liang, Controlled Electrochemical Oxidation for Enhancing the Capacitance of Carbon Nanotube Composites, Elsevier, Carbon 43 (2005) 1557–1583.
[42] H.M. Yasin, G. Denuault, D. Pletcher, Journal of Electroanalytical Chemistry 633 (2009) 327–332.
[43] C.R.K. Rao, D.C. Trivedi, Coordination Chemistry Reviews 249 (2005) 613–631.
[44] J. Zeng, C. Francia, C. Gerbaldi, M.A. Dumitrescu, S. Specchia, P. Spinelli, Journal of Solid State Electrochemistry 16 (2012) 3087–3096.
[45] P.V. Kamat, D.M. Guldi, F. DŚouza, Fullerenes and Nanotubes—The Building Blocks of Next Generation Nanodevices, Proceedings of the International Symposium on Fullerenes, Nanotubes, and Carbon Nanoclusters, The Electrochemical Society, 2003.
[46] A. Sarapuu, K. Helstein, K. Vaik, D.J. Schiffrin, K. Tammeveski, Electrochimica Acta 55 (2010) 6376–6382.
[47] T. Brülle, U. Stimming, Journal of Electroanalytical Chemistry 636 (2009) 10–17.
[48] C. Li, D. Wang, X. Wang, J. Liang, Carbon 43 (2005) 1557–1560.
[49] L. Wang, L. Ge, T.E. Rufford, J. Chen, W. Zhou, Z. Zhu, V. Rudolph, Carbon 49 (2011) 2022–2032.
[50] C.F. Brucker, Electron Spectroscopy: Theory, Techniques and Applications, vol. 4. C.R. Brundle and A.D. Baker (Eds.), Surface and Interface Analysis, Vol. 4, Academic Press, London, 1982, pp. i–ii.
[51] F. Onoue, K. Tsuji, ISIJ International 53 (2013) 1939–1942.
[52] M. Saitou, S. Teruya, S.M. Asadul Hossain, The Open Electrochemistry Journal 3 (2011) 1–5.
[53] S. Martin, P.L. Garcia-Ybarra, J.L. Castillo, International Journal of Hydrogen Energy 35 (2010) 10446–10451.
[54] J. Marie, R. Chenitz, M. Chatenet, S. Berthon-Fabry, N. Cornet, P. Achard, Journal of Power Sources 190 (2009) 423–434.
[55] M. Matsumoto, T. Miyazaki, H. Imai, The Journal of Physical Chemistry C 115 (2011) 11163–11169.